tween the phases is not strongly T-dependent in this temperature range.

Our analysis has focused on phase coexistence, where surface free energy plays the role of the chemical potential (*18*). One could achieve the same advantages in heteroepitaxial structures, such as quantum dots, by having them in equilibrium with a reservoir of controlled chemical potential μ_{res}, e.g., an ambient vapor at a specified partial pressure. For two-dimensional structures, elastic relaxation lowers the free energy relative to that of a uniform film for some range of island sizes. The chemical potential μ_0 of the uniform film plays the role of T_c here. For $\mu_{res} < \mu_0$, individual islands of a particular size are stable and do not grow. (The stable island size diverges as μ_{res} approaches μ_0.) As μ_{res} is decreased, the island size shrinks, until below some critical value μ_{min} the islands become unstable and disappear. This point defines the minimum stable island size, analogous to L_0. Thus, growth from a reservoir allows reversible and direct control of the island size, as well as the potential to circumvent kinetic limitations associated with coarsening.

Finally, we note that many properties of ensembles of domains are directly related to the energetics of an isolated domain. For example, not only isolated domains, but also groups of domains near equilibrium have a well-defined size, as shown in Fig. 4. Because the interaction between domains is repulsive, domains that are metastable when isolated ($L < 2.7\ L_0$) are necessarily metastable as part of a group. Thus, the configuration shown in Fig. 4 (with $L \approx 500$ nm) has a higher energy than the uniform "1 × 1" phase. Direct numerical computation of the elastic energy, including elastic interactions between domains, supports this conclusion. The hysteresis observed in the nucleation of 7 × 7 domains (*19*) is also explained by Eq. 3. Because the critical nucleus size is large and the nucleation kinetics are slow, nucleation near T_c is extremely unlikely. In practice, nucleation occurs only when T is well below T_c, where the critical nucleus size is small.

Our analysis of the stability of isolated 7 × 7 domains shows that size selection is directly linked to elastic relaxation at phase boundaries. For a range of temperatures above T_c, 7 × 7 domains are stable with well-defined equilibrium sizes. However, if the equilibrium size is less than about 2.7 L_0, the configuration is metastable, and conversion to the "1 × 1" phase is still energetically favorable, although kinetically hindered. The domain size must be very large—greater than about 550 nm—in order for elastic relaxation effects to offset the energy cost associated with the (unfavorable) 7 × 7 phase. Our analytical theory shows that the nucleation, formation energy, and size selection of isolated domains can be described in terms of a small number of measurable parameters. Knowledge of these parameters in strain-mediated self-assembly systems will be required for a detailed understanding and control of size selection at surfaces.

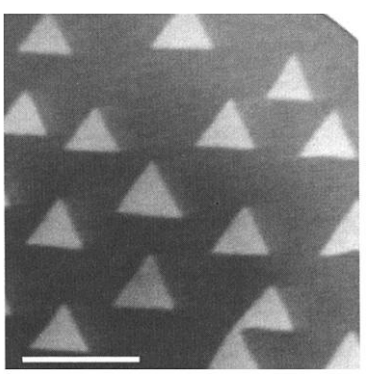

Fig. 4. Bright-field LEEM image (10 eV) of a near-equilibrium domain configuration above T_c. The bright areas indicate the 7 × 7 structure, whereas dark areas correspond to the "1 × 1" structure. All of the domains shown in the figure are metastable. The small variation in size among the domains is due to elastic interaction between the domains and a step outside the field of view. Scale bar, 1 μm.

References and Notes

1. V. A. Shchukin, D. Bimberg, *Rev. Mod. Phys.* **71**, 1125 (1999).
2. S. Aggarwal *et al.*, *Science* **287**, 2235 (2000).
3. V. I. Marchenko, *JETP Lett.* **33**, 382 (1981).
4. O. L. Alerhand, D. Vanderbilt, R. D. Meade, J. D. Joannopoulos, *Phys. Rev. Lett.* **61**, 1973 (1988).
5. D. Vanderbilt, *Surf. Sci. Lett.* **268**, L300 (1992).
6. K. O. Ng, D. Vanderbilt, *Phys. Rev. B* **52**, 2177 (1995).
7. M. Seul, D. Andelman, *Science* **267**, 476 (1995).
8. K. Takayanagi, Y. Tanishiro, S. Takahashi, M. Takahashi, *Surf. Sci.* **164**, 367 (1985).
9. J. B. Hannon, F. J. Meyer zu Heringdorf, J. Tersoff, R. M. Tromp, *Phys. Rev. Lett.* **86**, 4871 (2001).
10. In the striped geometry, the boundary length is independent of T. Consequently, the area fraction of each phase does not depend on the phase boundary creation energy.
11. We use the word "stable" to describe both stable and metastable domains above T_c. However, because the kinetics of nucleation are slow at the Si(111) surface, metastable domains are for all practical purposes stable.
12. F. M. Ross, R. M. Tromp, M. C. Reuter, *Science* **286**, 1931 (1999).
13. J. B. Hannon *et al.*, *Nature* **405**, 552 (2000).
14. E. Bauer, *Rep. Prog. Phys.* **57**, 895 (1994).
15. R. M. Tromp, M. Mankos, M. C. Reuter, A. W. Ellis, M. Copel, *Surf. Rev. Lett.* **5**, 1189 (1998).
16. R. D. Twesten, J. M. Gibson, *Phys. Rev. B* **50**, 17628 (1994). The surface stress of the 7 × 7 phase is more tensile than that of the "1 × 1" phase.
17. T. Hoshino *et al.*, *Phys. Rev. Lett.* **75**, 2372 (1995).
18. To make clear the correspondence with the familiar free energy $F = E - \mu N$, we could have written Eq. 1 as $F = E - \gamma_{1\times1} A$, where $E = \gamma_{7\times7} A + 3\beta L + U(L) + E_c$, and A is the domain area. The "reservoir" of area is the surrounding "1 × 1" phase, and its surface energy plays the role of the corresponding chemical potential μ.
19. C.-W. Wu, H. Hibino, T. Ogino, I. S. T. Tsong, *Surf. Sci.* **487**, 191 (2001).

20 September 2001; accepted 21 November 2001

Continuous Wave Operation of a Mid-Infrared Semiconductor Laser at Room Temperature

Mattias Beck,[1]* Daniel Hofstetter,[1] Thierry Aellen,[1] Jérôme Faist,[1] Ursula Oesterle,[2] Marc Ilegems,[2] Emilio Gini,[3] Hans Melchior[3]

Continuous wave operation of quantum cascade lasers is reported up to a temperature of 312 kelvin. The devices were fabricated as buried heterostructure lasers with high-reflection coatings on both laser facets, resulting in continuous wave operation with optical output power ranging from 17 milliwatts at 292 kelvin to 3 milliwatts at 312 kelvin, at an emission wavelength of 9.1 micrometers. The results demonstrate the potential of quantum cascade lasers as continuous wave mid-infrared light sources for high-resolution spectroscopy, chemical sensing applications, and free-space optical communication systems.

The mid-infrared portion of the spectrum, covering approximately the wavelength range from 3 to 12 μm, is sometimes referred to as "underdeveloped" because of its lack of convenient coherent optical sources. Especially when compared to the visible or near-infrared spectral range, where interband semiconductor lasers are now produced very economically with continuous wave (CW) output power of tens of milliwatts, this assertion holds true. In the mid-infrared, a new class of semiconductor lasers—intersubband quantum cascade (QC) lasers (*1*)—has become a promising alternative to interband diode lasers (*2*, *3*) in the past 7 years. In these devices, photon emission is obtained by electrons making optical transitions between confined energy lev-

[1]Institute of Physics, University of Neuchâtel, CH-2000 Neuchâtel, Switzerland. [2]Institute of Micro- and Optoelectronics, Department of Physics, Swiss Federal Institute of Technology, CH-1015 Lausanne, Switzerland. [3]Institute for Quantum Electronics, Department of Physics, Swiss Federal Institute of Technology, CH-8093 Zurich, Switzerland.

*To whom correspondence should be addressed. E-mail: Mattias.Beck@unine.ch

els. As such, QC lasers can be fabricated from wide-bandgap technologically mature semiconductors, and their emission wavelength can be tailored over a wide range by changing only the layer thicknesses. In addition, because their main nonradiative mechanism is optical phonon emission and because of the atomic-like joint density of states of intersubband transitions, QC lasers exhibit a gain that is weakly temperature dependent. As a result, QC lasers have demonstrated high mid-infrared output powers in pulsed operation up to temperatures above 400 K (*4*). However, CW operation of QC lasers based on standard designs has remained limited to cryogenic temperatures below 175 K (*5*). A recent active region design enabled CW operation up to 243 K (*6*), which is barely high enough to be maintained by a thermoelectric cooler.

Because the main nonradiative mechanism in mid-infrared interband lasers is Auger recombination, these devices exhibit a much stronger temperature dependence of the threshold current density, and CW operation is limited to temperatures below 225 K (*2*).

Although chemical sensing based on optical absorption has been successfully demonstrated with pulsed QC lasers (*7*), these systems are typically limited by the fairly wide emission linewidth of the QC laser (>500 MHz); high sensitivity can only be achieved with the narrow linewidth of a CW-operated device (*8*). Mid-infrared atmospheric optical communication systems (*9*, *10*), using QC lasers for data transmission through the two transparent atmospheric windows, will potentially benefit from light sources operating in CW mode at noncryogenic temperatures.

The limiting factor for CW operation of semiconductor lasers is the large heat dissipation. At high duty cycles, the temperature of the active region T_{act} is much higher than the heat sink temperature T_{sink}. In a simple model (*11*), the heat transport between active region and heat sink is characterized by the thermal conductance G_{th} per unit of area of the active region; that is, $T_{act} = T_{sink} + U \times J_{th}/G_{th}$ at threshold. Assuming a constant threshold voltage U and that the temperature dependence of the threshold current density J_{th} can be described by the phenomenological relation $J_{th} = J_0 \exp(T_{act}/T_0)$, the maximum CW operating temperature $T_{sink,max}$ of a QC laser is given by $T_{sink,max} = T_0 \times [\ln(T_0 G_{th}/J_0 U) - 1]$. A high value of the characteristic temperature T_0 is therefore an absolute necessity to achieve room-temperature CW operation. The large value of T_0 achieved in recent QC laser structures ($T_0 > 170$ K) results in a low temperature sensitivity of J_{th} and shows the potential of these devices for CW operation. However, the devices used in the early attempts to reach high-temperature CW operation (*12*, *5*) had a $J_0 U$ product of about 10 kW/cm^2. This value, corresponding to a threshold current density of ~5 kA/cm^2 at 300 K, is just too large to be evacuated from the active region when the laser is operated at high duty cycles, even assuming an idealized device geometry.

In addition, the actual core temperature is equal to $T_{act} = T_0 \times \ln(T_0 G_{th}/J_0 U)$ when the laser is operated at $T_{sink,max}$ (*13*), resulting in a temperature difference between the active region and the heat sink of T_0. For large T_0 values, the device might fail by thermal stress before reaching the temperature $T_{sink,max}$. For this reason, it is essential to (i) minimize the threshold current density and (ii) use a device geometry that minimizes thermal stress. To reduce the room-temperature threshold current density, active region designs based on a double-phonon resonance (*6*) and a bound-to-continuum transition (*14*) were recently developed. In these structures, the injection and extraction efficiency to and from the active region were significantly improved by means of wave function engineering. Additionally, growth conditions and the doping concentration of the active region were optimized. As a consequence, the pulsed threshold current density at 300 K dropped to a value as low as 3 kA/cm^2 (*6*).

We present QC lasers with an active region based on a double-phonon resonance and designed for a lasing transition at an energy of 135 meV (corresponding to a wavelength of 9.18 μm) between the upper and lower lasing states (levels 4 and 3 in Fig. 1A). The active region is composed of four quantum wells (QWs), which results in three coupled lower energy states (levels 1, 2, and 3) separated from each other by one phonon energy (*15*). The active region used a narrow QW-barrier pair just after the injection barrier [similar to the classical three-QW design (*16*)] that enhances the injection efficiency into the upper lasing level by increasing locally the magnitude of the upper state wave function (*12*). The observation of a clear resonant tunneling effect in structures with a three-QW active region demonstrated the effectiveness of this approach (*17*).

The fast intersubband scattering between the lowest subbands separated by an optical phonon energy should lead to a high population inversion in a three-QW active region

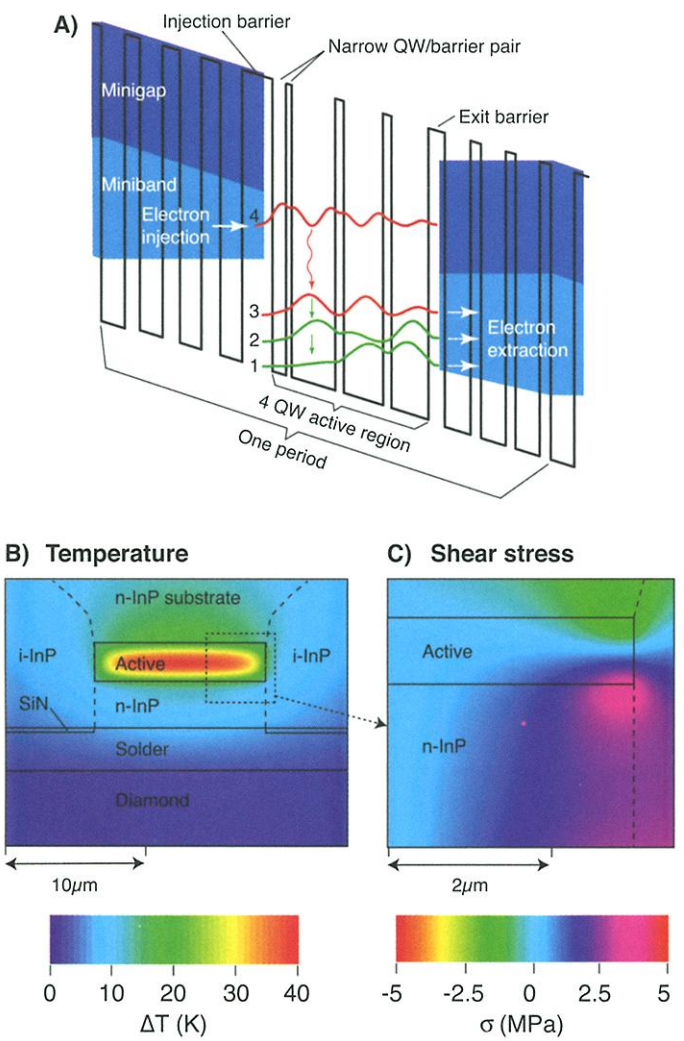

Fig. 1. (**A**) Schematic conduction-band diagram of one period of the laser core with moduli-squared relevant wave functions in the four-QW active region based on a double-phonon resonance. The red wavy arrow indicates the transition responsible for laser action, and green arrows represent optical phonon transitions. (**B**) Computed temperature contours around the active lasing region of the buried heterostructure QC laser at room temperature. The solid lines display the geometry of the different materials used in the simulation, and the dashed lines represent the geometry of the laser. (**C**) Computed thermally induced stress in the active region. The maximum stress occurs at the corner of the active region.

device, even at room temperature. However, the relatively slow measured tunneling time from the active region of about 2 ps (*18*, *19*) introduces an effective bottleneck to the electron transport, enhancing the lower laser state population. A model of the room-temperature electron kinetics in the active region (*20*), which included optical phonon emission and absorption from all points in *k*-space of the active region subbands, demonstrated that this bottleneck effect resulted in an effective lower state lifetime as long as 0.8 ps for a typical three-QW structure. The same computation also shows that the presence of an additional state in the active region (that is, level 1) allowing the emission of two optical phonons from the lower laser level decreases the lifetime of that level down to 0.5 ps. As a result, the computed ratio between the upper and lower state population increased from 1.9 for the three-QW structure to 2.8 in the double-phonon resonance structure, simultaneously decreasing the threshold current density and increasing the slope efficiency and maximum power, as was indeed observed (*6*).

Moreover, our devices were processed in a narrow-stripe, planarized, buried heterostructure geometry (*21*), in which the gain region was vertically and laterally buried within InP cladding layers, the geometry of which provides a number of advantages. The choice of a buried stripe greatly improves the heat transport by allowing heat flow from all sides of the active region. Additionally, the narrow-stripe geometry also decreases the total amount of strain that builds up in a material subjected to a very strong temperature gradient. Indeed, the results from a simulation, done with a commercial finite-elements differential equation solver (*22*), of both thermal transport and thermally induced stress lead to the same conclusions (Fig. 1, B and C). A thermal conductance of 820 W/Kcm^2 is predicted for a buried, 12-μm-wide, junction-down–mounted device, as compared to the calculated value of 510 W/Kcm^2 for a 28-μm-wide, ridge, junction-down–mounted device (*6*). Similarly, the maximum thermally induced shear stress that builds up at the edges of the active region (Fig. 1C) decreases from 22 MPa in the ridge device to 3.6 MPa for the buried structure.

Fabrication of the laser structure relied on molecular beam epitaxy for the growth of the lattice-matched InGaAs/InAlAs laser core on an InP substrate. The laser core consists of 35 periods, each comprising a partially n-doped injector region and the undoped four-QW active region, embedded in an optical waveguide formed on one side by the substrate and a lower InGaAs waveguide layer and on the other side by an upper InGaAs waveguide layer and the InP top cladding, which was grown by metalorganic vapor-phase epitaxy (MOVPE).

The lasers were fabricated into 12-μm-wide buried stripes by wet etching and selective MOVPE regrowth of i-InP using a SiO_2 mask. The devices were then cleaved into 750-μm-long lasers, soldered junction-down onto a diamond platelet, and finally facet-coated by a ZnSe/PbTe high-reflectivity (R = 0.7) layer pair.

The CW optical output power emitted from one facet (Fig. 2) was measured with a calibrated thermopile detector, which was mounted directly in front of the laser facet. At room temperature (292 K), the laser exhibited a threshold current of 390 mA (corresponding to a threshold current density J_{th} = 4.3 kA/cm^2 at a voltage bias U = 7.6 V) and a slope efficiency dP/dI of 101 mW/A (where P is optical power and I is current). This device emitted 13 mW of optical power from a single facet at a driving current of 550 mA, resulting in a wall plug efficiency of 0.55% per facet. Continuous wave operation was observed up to 312 K (39°C). At this temperature, the threshold current increased to 520 mA (J_{th} = 5.8 kA/cm^2), while still more than 1 mW of output power was emitted at 550 mA. The electrical transport characteristics of the device (inset of Fig. 2) display the expected discontinuity of the differential resistance at threshold (390 mA).

A laser with the same cavity length but a slightly larger stripe width of 15 μm emitted 17 mW per facet at a drive current of 600 mA at room temperature. This device could be operated up to 311 K, with a maximum optical power of 3 mW and a threshold current of 540 mA (J_{th} = 4.8 kA/cm^2).

The performance of these buried heterostructure devices demonstrates the results of the thermoelastic predictions. Although the junction-down–mounted, 28-μm-wide, conventional ridge lasers failed systematically at 4 kA/cm^2 (*6*), the 12-μm-wide buried lasers discussed in this paper supported more than 6 kA/cm^2.

The emission frequency ν of a QC laser can be tuned over a small range of a few cm^{-1} by changing the current and temperature. The CW spectral properties were analyzed with a Fourier transform infrared spectrometer. The emission spectra (Fig. 3A) collected at a constant heat sink temperature of 292 K and various currents between 395 and 530 mA reveal frequency tuning from 1096.74 cm^{-1} to 1094.54 cm^{-1}, linear with the electrical input power (inset of Fig. 3A). At a fixed current of 530 mA, the emission frequency of the laser shifts from 1094.54 cm^{-1} at 292 K to 1092.90 cm^{-1} at 313 K (Fig. 3B). The measured center frequencies are well fitted by a linear function (inset of Fig. 3B) with a tuning coefficient of $\Delta\nu/\Delta T$ = −0.078 cm^{-1}/K. Single mode emission was observed for this particular device over the whole investigated current and temperature range, with a side mode suppression ratio better than 30 dB. This rather surprising fact can be explained by a small defect within the laser cavity, as indicated by an intensity modulation of the subthreshold Fabry-Perot fringes at twice the cavity mode spacing.

Assuming that the emission frequency ν is a function only of the temperature of the active region, we can deduce a thermal resistance R_{th} of the device from the variation of the emission frequency (*11*) with $R_{th} = \left(\frac{\Delta T}{\Delta P}\right) = \left(\frac{\Delta \upsilon}{\Delta P}\right) \times \left(\frac{\Delta \upsilon}{\Delta T}\right)^{-1}$. Inserting the above tuning rates, we get a thermal resistance of 19.4 K/W in the range between 292 K and 313 K (corresponding to a thermal conductance G_{th} of 574 W/Kcm^2). This R_{th} value is higher than the calculated one (13.6 K/W), most likely because the thermal interface resistance was not included in our simulation.

The dependence of the threshold current density J_{th} on the actual core temperature T_{act} of the laser is measured in pulsed mode at low duty cycles, where heating effects are negligible (that is, $T_{act} \sim T_{sink}$). At 292 K, we measured a pulsed J_{th} as low as 3.1 kA/cm^2 (compared to 4.3 kA/cm^2 in CW operation) for the 12-μm-wide device, corresponding to a threshold current I_{th} = 280 mA. The experimental pulsed threshold current densities (Fig. 4) can be fitted by the expression $J_{th} = J_0 \exp(T_{act}/T_0)$ with a T_0 = 171 K and J_0 = 560 A/cm^2.

The temperature dependence of the CW threshold current density can be computed from the data in pulsed operation, using a slightly modified model that takes into account the change in applied voltage with

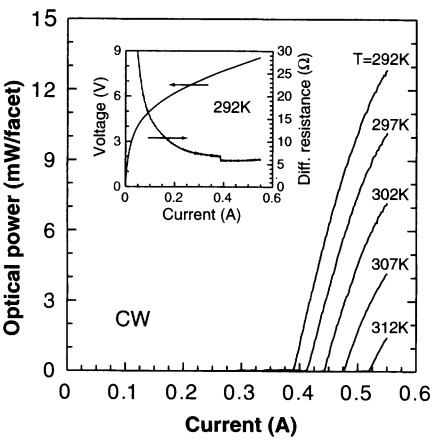

Fig. 2. CW optical power from a single laser facet as a function of drive current for various heat sink temperatures. The laser is 0.75 mm long and 12 μm wide. The power was measured with near-unity collection efficiency and a calibrated thermopile detector. **(Inset)** Electrical transport characteristics of the laser at 292 K: bias voltage as a function of injection current and differential resistance deduced from the *V-I* curve.

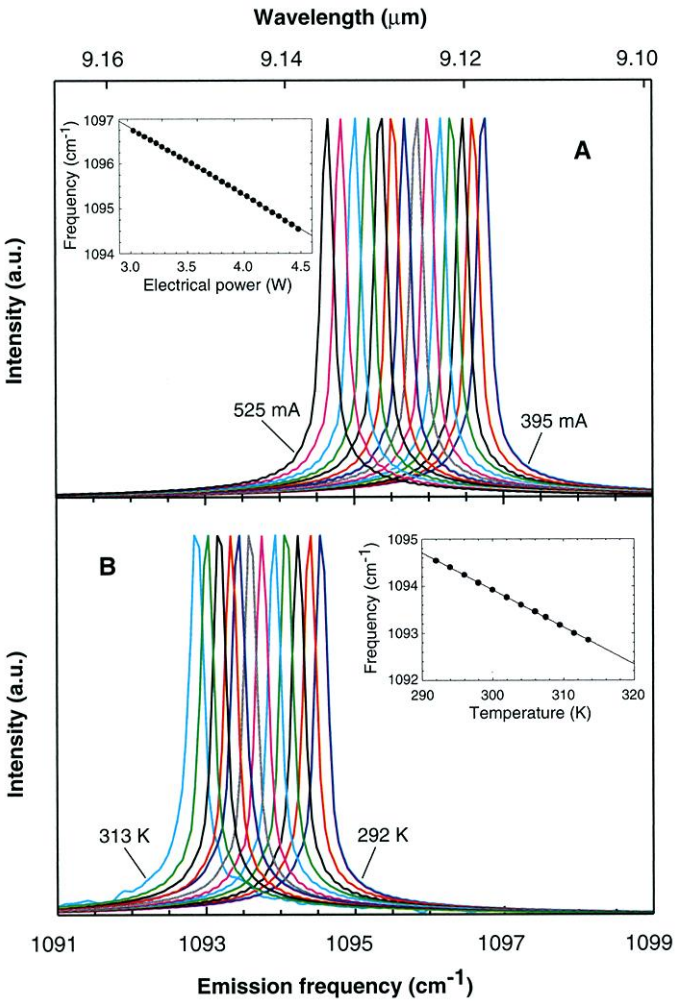

Fig. 3. (**A**) High-resolution (0.125 cm^{-1}) CW spectra as a function of injection current. The emission spectra were measured at a constant temperature of 292 K for various drive currents ranging from 395 up to 525 mA in steps of 10 mA. The curves are normalized to the emission spectrum measured at 525 mA and plotted in linear scale. a.u., arbitrary units. (**Inset**) Emitted peak frequency in dependence of the electrical input power at constant temperature. We deduced a linear tuning coefficient of $\Delta\nu/\Delta P = -1.51$ cm^{-1} W^{-1}. (**B**) Series of CW emission spectra as a function of temperature at a constant drive current of 530 mA. The temperature varies from 292 to 313 K. The curves are normalized to the emission spectrum measured at 292 K. (**Inset**) Measured temperature dependence of the center emission frequency at a fixed injection current.

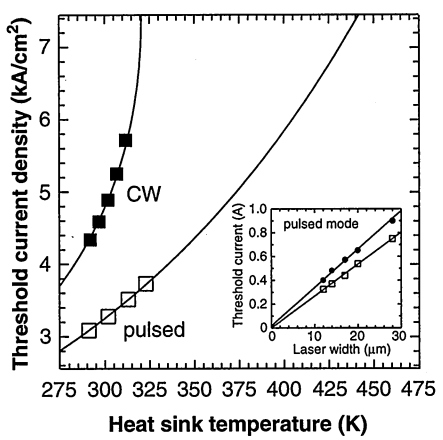

Fig. 4. Threshold current density as a function of heat sink temperature. The experimental pulsed J_{th} (open symbols) are fitted by the function $J_{th} = J_0 \times \exp(T/T_0)$, with $T_0 = 171$ K and $J_0 = 560$ A/cm² (lower solid line). Solid symbols represent the CW threshold current densities of the same device. The upper solid line is the computed dependence of the CW threshold current density on the heat sink temperature, using the modified model with a current-dependent voltage bias. (**Inset**) Pulsed threshold current as a function of laser width. The threshold currents of the facet-coated devices (open symbols) are ~20% lower as compared to the threshold currents of the same devices but without facet coatings (solid symbols).

injected current (*23*) and uses the thermal conductance G_{th} obtained from the spectral measurements. The calculated J_{th} curve fits well with the experimental CW J_{th} values (solid symbols in Fig. 4). The data also show that, at 292 K, the temperature difference $\Delta T = T_{act} - T_{sink}$ between laser core and heat sink is 58 K at threshold and increases to 87 K at the maximum injected current. With this modified model, we calculate a maximum CW operating temperature $T_{sink,max} = 321$ K and a $\Delta T = 119$ K at that operating temperature.

The threshold currents of our buried heterostructure QC lasers scale accurately with the laser stripe width (inset of Fig. 4). It means that our device architecture does not introduce additional lateral waveguide losses or current leakage paths.

The far-field distributions in the two directions parallel and perpendicular to the grown layers exhibited a Gaussian profile with far-field angle of 40° full width at half maximum in the in-plane direction and 80° perpendicular to the layers, proving that the device oscillates in its fundamental lateral and transverse mode.

Fundamental intersubband processes did not limit the device performance. Assuming the measured waveguide loss value of 10 cm^{-1} (*24*) and in the limiting case of unity injection efficiency, the threshold current density of our QC laser should be 2.1 kA/cm² (*25*), which is significantly lower than the measured value (3.1 kA/cm²). We believe that further improvements in active region design and growth conditions should bring us closer to this limiting case. In addition, a reduction of the stripe width to 5 to 6 μm should further improve G_{th} (by about 20%) while still maintaining a large value of confinement factor. In that case, our model predicts a maximum CW operating temperature of $T > 370$ K.

References and Notes

1. J. Faist *et al.*, *Science* **264**, 553 (1994).
2. Z. Feit *et al.*, *Appl. Phys. Lett.* **68**, 738 (1996).
3. W. W. Bewley *et al.*, *Appl. Phys. Lett.* **76**, 256 (2000).
4. C. Gmachl *et al.*, *IEE Electron. Lett.* **36**, 723 (2000).
5. C. Gmachl *et al.*, *IEEE Photon. Technol. Lett.* **11**, 1369 (1999).
6. D. Hofstetter *et al.*, *Appl. Phys. Lett.* **78**, 1964 (2001).
7. K. Namjou *et al.*, *Opt. Lett.* **23**, 219 (1998).
8. A. A. Kosterev *et al.*, *Opt. Lett.* **24**, 1762 (1999).
9. R. Martini *et al.*, *IEE Electron. Lett.* **37**, 111 (2001).
10. S. Blaser *et al.*, *IEE Electron. Lett.* **37**, 778 (2001).
11. J. Faist *et al.*, *IEEE J. Quantum Electron.* **34**, 336 (1998).
12. J. Faist *et al.*, *Appl. Phys. Lett.* **68**, 3680 (1996).
13. This follows from the derivation of the equation $T_{sink} = T_{act} - U \times J_0 \exp(T_{act}/T_0)/G_{th}$.
14. J. Faist *et al.*, *Appl. Phys. Lett.* **78**, 147 (2001).
15. The layer sequence of one period, in nanometers, from left to right in Fig. 1A and starting with the injection barrier, is as follows: **4.0**/1.9/**0.7**/5.8/**0.9**/5.7/**0.9**/5.0/**2.2**/3.4/**1.4**/3.3/**1.3**/3.2/**1.5**/3.1/**1.9**/3.0/**2.3**/2.9/**2.5**/2.9, where InAlAs barrier layers are in bold, InGaAs well layers are in roman, and n-doped layers (2×10^{17} cm^{-3}) are underlined.
16. The three-QW active region design has widely been used in QC devices. Its schematic band structure roughly corresponds to the first three QWs, counting from the injection barrier, of the active region in Fig. 1A. The corresponding energy spectrum is similar to the double-phonon resonance device but without the $n = 1$ state.
17. C. Sirtori *et al.*, *IEEE J. Quantum Electron.* **34**, 1722 (1998).
18. J. Faist *et al.*, *Phys. Rev. Lett.* **76**, 411 (1996).
19. S. Blaser *et al.*, *IEEE J. Quantum Electron.* **37**, 448 (2001).
20. The electron kinetic computation assumed that the electrons interacted with a thermal distribution of bulk optical phonons at 300 K. The emission (e) and absorption (a) lifetimes from the active region states are (in ps): $\tau_{43e} = 1.88$, $\tau_{43a} = 9.3$, $\tau_{42e} = 1.92$, $\tau_{42a} = 8.5$, $\tau_{41e} = 2.51$, $\tau_{41a} = 11.5$, $\tau_{32e} = 0.73$, $\tau_{32a} = 3.8$, $\tau_{31e} = 0.23$, $\tau_{31a} = 2.3$, $\tau_{21e} = 0.28$, $\tau_{21a} = 2.7$ ($n = 4$ is the upper laser level). The lifetime for intrasubband processes is $\tau_{em} = 0.14$ ps for emission and $\tau_{abs} = 0.55$ ps for absorption of optical phonons. The escape time $\tau_{esc} = 2$ ps was the same for all the lower ($n = 1..3$) states.
21. M. Beck *et al.*, *IEEE Photon. Technol. Lett.* **12**, 1450 (2000).
22. The simulation of the thermoelastic behavior of the device was done with a commercial finite-elements software package (PDease2D). Room-temperature thermal conductivities were used. The elastic properties of the semiconductor were approximated by

isotropic elastic constants with the Young modulus E = 84 GPa and Poisson's ratio ν = 0.3.
23. At 292 K, the voltage-current (V-I) curve above threshold was modeled by $U = U_0 + R \times I$, with U_0 = 5.34 V and R = 5.87 ohm.
24. M. Rochat, M. Beck, J. Faist, U. Oesterle, *Appl. Phys. Lett.* **78**, 1967 (2001). This value agrees with the one computed by a Drude model.
25. Computed with the formula used in (*11*), with the following parameters (at 300 K): period length L_p = 60 nm; dipole matrix element z = 3 nm; intersubband lifetimes τ_{32} = 1.45 ps, τ_3 = 0.52 ps, and an effective τ_2 = 0.5 ps; overlap factor Γ_p = 0.0183; broadening of the transition $2\gamma_{32}$ = 22 meV; and effective index n_{eff} = 3.2 and $n_{th} = 8 \times 10^8$ cm^{-2}.
26. We gratefully acknowledge M. Ebnöther for technical assistance with the lateral InP regrowth. Financially supported by the Swiss National Science Foundation and the Science Foundation of the European Community under IST project SUPERSMILE.

20 September 2001; accepted 20 November 2001
Published online 20 December 2001;
10.1126/science.1066408
Include this information when citing this paper.

Remarkably Selective Iridium Catalysts for the Elaboration of Aromatic C–H Bonds

Jian-Yang Cho, Man Kin Tse, Daniel Holmes, Robert E. Maleczka Jr., Milton R. Smith III*

Arylboron compounds have intriguing properties and are important building blocks for chemical synthesis. A family of Ir catalysts now enables the direct synthesis of arylboron compounds from aromatic hydrocarbons and boranes under "solventless" conditions. The Ir catalysts are highly selective for C–H activation and do not interfere with subsequent in situ transformations, including Pd-mediated cross-couplings with aryl halides. By virtue of their favorable activities and exceptional selectivities, these Ir catalysts impart the synthetic versatility of arylboron reagents to C–H bonds in aromatic and heteroaromatic hydrocarbons.

Carbon-carbon bonds are the molecular "bricks and mortar" from which diverse architectures in living organisms and man-made materials are constructed. As the field of organic chemistry has evolved, numerous methods for carbon-carbon bond construction have been developed, ranging from classic examples, like the Diels-Alder reaction, to more recent metal-catalyzed processes, such as olefin polymerizations and metatheses.

Biaryl subunits and their heteroaromatic analogs are abundant in natural and synthetic materials, and controlled methods for linking aromatic rings via C–C sigma bonds have long been pursued by organic chemists. Activity in this regard intensified in the late 1970s, during which Pd-catalyzed methods for C–C bond construction emerged (*1*). First disclosed by Miyaura and Suzuki, the Pd-catalyzed coupling of an arylboronic acid and an aryl halide (Y = OH, X = halide)

$$Ar^1-BY_2 + Ar^2-X \xrightarrow{[Pd]} Ar^1-Ar^2 + X-BY_2 \quad (1)$$

has become a method of choice for preparing biaryls because it is performed under mild conditions that are tolerant of diverse functionality (*2*). Subsequent developments in metal-catalyzed cross-couplings of organoboron compounds and organic halides have yielded practical C–C bond forming strategies that complement existing methodology (*3*). Today, the Miyaura-Suzuki reaction is routinely applied in high-throughput screening for drug discovery (*4*), in the final steps of convergent natural product syntheses (*5*), and in the synthesis of conjugated organic materials (*6*).

Arylboron reagents are typically synthesized in a multistep process such as that depicted in Fig. 1A. Shorter routes that avoid undesirable halogenated aromatic intermediates would be attractive. To this end, theoretical estimates of B–H and B–C bond enthalpies gave credence to organoborane synthesis via the thermal dehydrogenative coupling of B–H and C–H bonds (Fig. 1B) (*7*). Some key steps in putative catalytic cycles for this process had been established in reports by Hartwig and co-workers (*8*) and Marder and co-workers (*9*) of stoichiometric borylations of arenes, alkenes, and alkanes by metal boryl complexes (M–BR_2). Whereas Hartwig and co-workers developed elegant photochemical methods for hydrocarbon borylation using catalytic amounts of metal complexes (*10*), thermal, catalytic borylations of unactivated hydrocarbons were not documented before our report in 1999 (*11*).

Our initial work was inspired by Bergman's (*12*) and Jones's (*13*) fundamental studies of hydrocarbon (R–H, where R = alkyl or aryl) activation by $Cp^*(PMe_3)M^I$ intermediates (where M = Ir, Rh; $Cp^* = \eta^5$-C_5Me_5), which produce $Cp^*(PMe_3)M^{III}(H)(R)$ where M–H and M–R bonds result from R–H scission. While investigating stoichiometric B–C bond formation in reactions between $Cp^*(PMe_3)Ir(H)(Ph)$ and pinacolborane (HBPin), we noticed that substantial quantities of arylboron products were produced from catalytic solvent activation. The major metal-containing product in this reaction, $Cp^*(PMe_3)Ir(H)(BPin)$ (**1**), was a precatalyst for benzene borylation with an effective turnover number (TON) corresponding to the formation of three molecules of Ph-BPin per molecule of **1** (*11*). Subsequently, Hartwig and co-workers reported alkane and arene borylations with the use of much more active Rh precatalysts, such as $Cp^*Rh(\eta^4$-$C_6Me_6)$ (**2**) (*14*).

A comparison of precatalysts **1** and **2** in borylations of various substituted arenes revealed that the Ir system was more selective toward arene C–H activation (*15*). Given the importance of selectivity in chemical synthesis, these findings spurred a detailed investigation of the original Ir system.

Compound **1** was stable in benzene solutions after prolonged thermolysis, which eliminates several mechanistic possibilities, including PMe_3 dissociation to generate $Cp^*Ir(H)(BPin)$, an analog of proposed intermediates in the Rh system. However, added PMe_3 strongly inhibited catalysis where HBPin was present. This finding raised the possibility that small quantities of phosphine-free Ir^V species could be active. Because $Cp^*IrH_{4-x}(BPin)_x$ species (where x = 1, 2) form in the thermolysis of Cp^*IrH_4 and HBPin (*16*), anisole borylations with identical loadings of Cp^*IrH_4 and **1** were compared. From this experiment, $Cp^*IrH_{4-x}(BPin)_x$ intermediates could be eliminated because they are not kinetically competent for catalysis and because the borylation regioselectivities for Cp^*IrH_4 and **1** differed substantially (*17*).

Exclusion of a simple phosphine dissociative pathway narrows the plausible catalysts to two choices: (i) Ir phosphine species arising from Cp* loss or (ii) species where both Cp* and PMe_3 have been lost. The latter possibility is

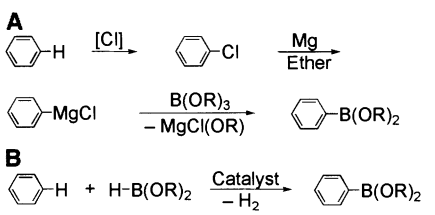

Fig. 1. (**A**) Traditional and (**B**) direct routes to arylboronic esters from aromatic hydrocarbons.

Department of Chemistry, Michigan State University, East Lansing, MI 48824, USA.

*To whom correspondence should be addressed. E-mail: smithmil@msu.edu